Experimental Mechanics (2018) 58:207–221
DOI 10.1007/s11340-017-0334-7

Experimental investigation of the coupled magneto-mechanical response in magnetorheological elastomers

L. Bodelot[1] · **J.-P. Voropaieff**[1] · **T. Pössinger**[1]

Received: 19 April 2017 / Accepted: 21 August 2017 / Published online: 18 September 2017

Abstract Magnetorheological elastomers (MREs) are materials made of a soft elastomer matrix filled with magnetizable particles. These flexible composites that deform in response to an externally applied magnetic field are of special interest in advanced engineering applications such as actuators, artificial muscles or shape control. However, no systematic characterization of their coupled response has been undertaken so far, thus limiting the efficient design of MRE-based devices. In this study, we propose a framework—relying on both specially designed samples and a dedicated experimental setup—to characterize experimentally the coupled magneto-mechanical response of MREs since magnetization within the sample is nearly uniform and structural-dependent effects are minimized. The influence of particle content and arrangement within the composite are particularly studied and the corresponding experimental results give some insight into the underlying microstructural mechanisms that are responsible for the macroscopic deformation of MREs under combined magnetic and mechanical loading conditions. Such data is crucial for the design of new MRE composite materials in which the microstructure is optimized (to have the largest coupling effect with minimal energy input).

Keywords Magneto-mechanical response · Image analysis · Hall probes · Magnetorheological elastomers · Polymers · Magneto-mechanical couplings

Electronic supplementary material The online version of this article (https://doi.org/10.1007/s11340-017-0334-7) contains supplementary material, which is available to authorized users.

✉ L. Bodelot
laurence.bodelot@polytechnique.edu

[1] Laboratoire de Mécanique des Solides, Ecole Polytechnique, CNRS, Université Paris-Saclay, 91128 Palaiseau, France

Introduction

This work pertains to the technologically important area of active materials (also commonly named smart materials). These can be broadly defined as materials in which a stimulus from a given physical domain (mechanical, electrical, magnetic, thermal, etc.) generates a response belonging to another domain. As a branch of active materials, magnetorheological elastomers consist of a non-magnetic elastomeric matrix into which magnetically polarizable particles are mixed [1]. Rigbi and Jilken [2] were the first to conduct tests on MREs and to describe the previously unknown magneto-mechanical effects. Indeed, the soft characteristics of the matrix combined with the magnetic properties of the particles allow these flexible composites to both deform largely and to alter their stiffness promptly in response to a rather low external magnetic field. These characteristics make MREs of special interest in a variety of advanced engineering applications such as tunable damping, actuators, artificial muscles or shape control (see reviews by Hamrock [1] and Bustamante [3]).

Considering the variety of possible matrix-filler combinations, many experimental studies have been dedicated to the composition and processing of MREs along with the investigation of the obtained microstructures [4–6]. Among all possible matrix materials, silicone rubbers stand out due to their excellent processability, their good thermal and aging properties, as well as their low elastic modulus that tends to facilitate the magneto-mechanical interaction [7, 8]. As far as particles are concerned, micron-sized iron particles are the most common since they exhibit high magnetic susceptibility and high saturation magnetization, thus providing high inter-particle interaction forces as well as low remanent magnetization (a property required to obtain quick and reversible control by the magnetic field in MRE devices [9]). Extensive studies have also been conducted to investigate the influence of an external

magnetic field on the damping properties of MREs such as storage, loss and viscoelastic moduli [10–12]. In particular, their performance as tunable vibration absorbers and tunable stiffness devices have been analyzed and prototypes have been developed [13–18].

In contrast and despite a potential for slower time response applications in artificial muscles or shape control, only a handful of experimental studies have focused on characterizing the coupled magneto-mechanical behavior of MREs under low-rate loadings. One of the difficulties lies in the fact that standard mechanical testing methods yielding uniform mechanical fields within the elastomer test specimen have to be combined with externally applied magnetic loadings that induce a uniform magnetic field distribution inside the sample. Additionally, in order to analyze the magneto-mechanical couplings, both magnetic and mechanical quantities have to be measured during sample deformation. Since the first experimental studies regarding MREs often approached their behavior without the prospect of providing data for magneto-mechanical models, one only can find in the literature a large number of tests (quasi-static, large strains, high magnetic field) for various MRE materials and samples with measurements of the magnetic properties—if done at all—performed separately from mechanical ones (i.e. no coupling). Some studies indeed focused on the deformation of MREs under purely magnetic loading [19, 20]. Other studies explored the mechanical response of MREs under magnetic fields but performed experiments in which either the magnetic field was not uniform [4, 21–24] and/or in which there was no access to all mechanical quantities [25–29]. Additionally, important mechanical effects arising in filled elastomers—namely the Mullins effect [30–33] and interfacial debonding between the matrix and the particles [34–36]—are ignored in these studies and may explain some of the unexpected and unrepeatable results [19, 37].

Hence there exist, to our knowledge, no precise and complete characterization of the fully-coupled magneto-mechanical response of MREs, hindering the further design of MRE-based devices and the validation of magneto-mechanical models. Through this work, we aim to understand the macroscopic response of MREs under combined magnetic and mechanical loading conditions. For this purpose, we have developed a framework for characterizing experimentally the coupled magneto-mechanical behavior of MREs up to large strains and up to high magnetic fields, relying on both specially designed samples and a dedicated experimental setup that provides precise in-situ coupled data while the magnetic field remains nearly uniform within the sample. The results thereby obtained on MREs with different particle volume fractions provide insight into the underlying microstructural mechanisms responsible for the macroscopic deformation of MREs under coupled loading conditions.

Samples

Due to the scarcity of coupled magneto-mechanical characterization existing in the literature, there has been so far no reference sample specially devised for carrying a coupled characterization. Considering this is the main goal of the present study, the crucial topic of the sample shape is addressed in what follows after introducing the relevant magnetic quantities arising in magnetizable bodies. Furthermore, aspects pertaining to material selection and fabrication protocols for both isotropic and transversely isotropic MRE samples are presented.

Magnetic Quantities Involved in Ferromagnetic Bodies

In vacuum, the magnetic field $\mathbf{b}_0 = \mu_0\,\mathbf{h}_0$ corresponds to the externally applied magnetic field intensity $\mathbf{h}_0$ multiplied by the magnetic permeability of the free space $\mu_0 = 4\pi\ 10^{-7}$ [N/A^2]. If a finite ferromagnetic body is exposed to the excitation field $\mathbf{h}_0$, the body becomes magnetized and generates a perturbation field $\mathbf{h}_1$ [38]. The macroscopic magnetic constitutive relation can then be defined, following the SI system, as

$$\mathbf{b} = \mu_0\,(\mathbf{h}_0 + \mathbf{h}_1 + \mathbf{m}) = \mu_0\,(\mathbf{h} + \mathbf{m}), \tag{1}$$

where $\mathbf{b} = \mathbf{b}_0 + \mathbf{b}_1$ is the total magnetic field (or magnetic induction) expressed in Tesla [T = N/A.m], and $\mathbf{b}_1 = \mu_0\,(\mathbf{h}_1 + \mathbf{m})$ is the magnetic perturbation field. The state of magnetic polarization within the body is described by the magnetization field $\mathbf{m}$ [A/m]. The quantity $\mathbf{h} = \mathbf{h}_0 + \mathbf{h}_1$ is the total $\mathbf{h}$-field (or magnetic field intensity) expressed in [A/m]. The nonlinear relation between $\mathbf{h}$ and $\mathbf{m}$ for a ferromagnetic bulk material can be determined experimentally and usually takes the form of a hysteresis loop. The dimensionless volume susceptibility χ [−] corresponds to the initial slope of the $\mathbf{m} - \mathbf{h}$ curve. Here it is important to note that even if the externally applied field $\mathbf{h}_0$ is perfectly uniform, a ferromagnetic body can create magnetic field gradients within itself. Indeed, since the magnetostatic field equations and the corresponding boundary conditions prescribe the field distribution within a body, the resulting magnetization within a body strongly depends on its geometry.

Sample Shape for Coupled Magneto-Mechanical Testing

Samples shapes for the evaluation of mechanical material properties are devised to achieve a uniform state of stress in the gage area of the sample far away from the clamping. This yields the well-known dog-bone shape samples for tensile testing. For elastomers, the norms (ASTM D412/ISO 37 [39, 40]) only propose dog-bone shape samples with a rectangular cross-section since rubber specimens are often punched out of large sheets. However, as mentioned earlier, the shape of a body influences

the distribution of the total magnetic field **b** even when submitted to a uniform external magnetic field $\mathbf{b}_0$. A numerical simulation, performed with the Finite Element Method (FEM) software ANSYS and reported in Fig. 1(a), indeed confirms that the magnetic perturbation field $\mathbf{b}_1$ (and thus **b** when the sample is magnetized by a uniform external magnetic field $\mathbf{b}_0$) is not uniform in the gage area of a dog-bone shape sample with a rectangular cross-section. Note that these simulations, run at the stage of sample design, are mainly for illustrative purposes. Hence we consider here the simplified case of a ferromagnetic bulk that does not deform under magnetic field—even though some elaborate models proposed in the literature could account for magneto-mechanical couplings in MREs (e.g. [29, 41, 42])—and present normalized data. Following common usage in tensile testing of metals (ASTM E8/ISO 6892 [43, 44]), the same type of dog-bone shape sample—but with a circular cross-section—could be used since it does not affect the uniformity of the mechanical quantities in the gage area. The dimensions of this sample are given in Fig. 2(a). In this case, the FEM simulation reported in Fig. 1(b) shows that the magnetic perturbation field $\mathbf{b}_1$ is now uniform in the gage area when the sample is uniformly magnetized transverse to its longitudinal axis. Nevertheless, this sample still exhibits a non-uniform magnetic field **b** in its heads since only magnetic bodies of ellipsoidal (or as a subset, spherical) shapes can exhibit uniform magnetization **m** and perturbation $\mathbf{h}_1$ (and hence uniform total magnetic field **b**) throughout their whole body [38, 45]. Though in mechanics uniformity is sufficient in the gage area to ensure proper material characterization, it has to be verified experimentally whether this is also the case when magneto-mechanical coupling is considered as the magnetization of the heads may influence the sample's behavior. Based on the design of the dog-bone shape sample with a circular cross-section (Fig. 2(a)), the sample heads are replaced by non-magnetic 3D–printed plastic insets while only the cylindrical gage area is made of MRE and terminated at both ends by an ellipsoidal cap (see Fig. 2(b), (c)). This brings the body of the sample as close as possible to an ellipsoid while retaining the uniformity of mechanical quantities in the gage area under mechanical loading. An FEM simulation, reported in Fig. 1(c), confirms that the magnetic perturbation field $\mathbf{b}_1$ is almost uniform in the nearly ellipsoidal MRE body of this modified sample since the heads do not interact with the magnetic field. Before looking at the impact of this modification on the magneto-mechanical coupling, it is first verified whether it affects the mechanical response. To this end, purely mechanical tests are performed on fully-MRE dog-bone shape samples with a circular cross-section and on samples with a nearly ellipsoidal MRE body and plastic heads, for each particle content considered in this study, expressed as *phr* (per hundred rubber, i.e. mass of filler particles per hundred parts of raw compounded polymer mass, see *Materials* section for additional information). All the corresponding upload parts of the 3rd stabilized cycles (see *Experimental Methods* for details on the testing protocol) are presented in Fig. 3(a). The curves reveal that the mechanical responses of the tested samples are only identical up to a certain threshold, after which the latter sample exhibits a loss of carrying load capacity due to debonding at the interface between the soft MRE body and the stiffer plastic heads. The threshold is the lowest for the highest particle content; but for all particle contents studied here, the fully-MRE dog-bone shape sample with a circular cross-section and the sample with a nearly ellipsoidal MRE body and plastic heads show within experimental error the same mechanical response up to a 1.4 stretch. To address the question of the magneto-mechanical coupling, the stress response under purely magnetic loading (up to $\mathbf{b}_0$ = 0.8 T) is monitored for the two aforementioned geometries in the case of the lowest particle content considered in the study (70 *phr*), while they are held fixed in the uniform magnetic field that is applied transversely to their longitudinal axis within the dedicated setup described in the *Experimental Methods* section. The corresponding results, reported in Fig. 3(b), show that the stress exerted by the sample is much higher in the case of the fully MRE dog-bone shape sample with a circular cross-section than in the case of the dog-bone shape sample with a nearly ellipsoidal MRE body and plastic heads. This confirms the large contribution of the magnetization gradients present within the MRE heads to the magneto-mechanical response of the sample. Hence, when magnetic fields are at play, uniformity shall be achieved within the whole sample and not only in the gage area of the studied sample, since the whole sample contributes to the coupled magneto-mechanical response. As a result, in order to perform a coupled magneto-mechanical testing of MREs, fully-MRE dog-bone shape samples with a circular cross-section will be used for purely mechanical tests up to large stretches, while samples with a nearly ellipsoidal MRE body and plastic heads will be used for coupled experiments provided that the overall stretch remains below the 1.4 nominal stretch (40% nominal strain) threshold identified earlier (which still goes largely beyond the domain of small strains).

Materials

In order to maximize the magneto-mechanical coupling, the selected matrix material is a very soft and stretchable silicone elastomer: Ecoflex 00–20 from Smooth-On Inc., USA. This elastomer is a room temperature, two-part addition-cured platinum-catalyzed system (RTV-2) with a mixed density ρ_{sil} of 1070 kg / m^3 and a mixed viscosity of 3 Pa.s that offers a good compromise between good dispersion when mixing, easy pouring and minimal settling of particles during accelerated curing. The filler phase is carbonyl iron powder (CIP) SM from BASF. This powder is made of spherical particles having a median diameter of 3.5 μm and it contains up to 99.8% of Fe with low amounts of C, N and O. It is considered magnetically "soft" as it does not retain magnetization once the magnetic field is turned off. Since soft iron is also known to have a low

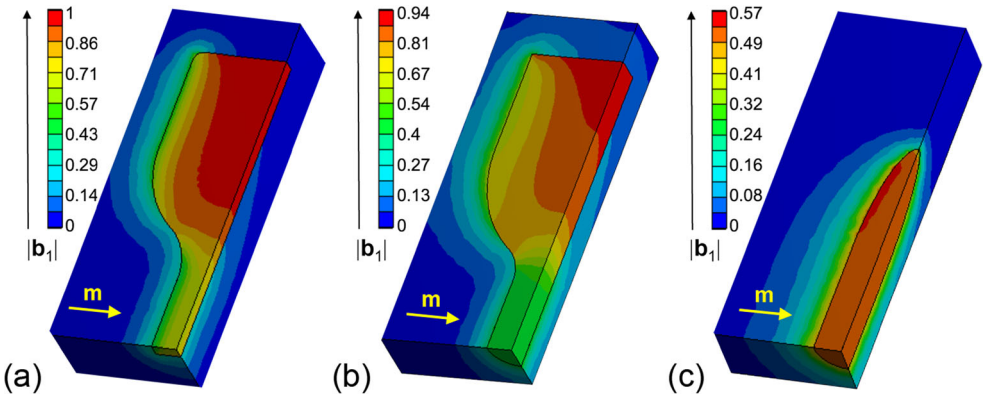

Fig. 1 3D FEM simulations in ANSYS showing the normalized magnitude of the magnetic perturbation field $|b_1|$ in different types of ferromagnetic samples uniformly magnetized transversely to their longitudinal axis (**a**) Dog-bone shape sample with rectangular cross-section (**b**) Dog-bone shape sample with circular cross-section (**c**) Cylinder closed with two half-ellipsoids

coercivity and a magnetic saturation $\mu_0 m_s = 2.1$ T [46], these particles are good candidates for MRE applications with optimal coupling. According to the manufacturer, the bulk density ρ_{bulk} is between 1500 and 2500 kg/m^3 in the form of powder, but this density becomes irrelevant once the particles are mixed in the viscous liquid elastomer. Hence the density commonly considered in the MRE literature is taken as that of solid iron metal (e.g. [47]), 7874 kg/m^3, or slightly lower than that of iron (e.g. [48])—probably to account for the exact chemistry of the particles. In practice during fabrication, the different elements of the compound are weighed and one actually works with m_{CIP}, m_A and m_B corresponding to the mass of CIP particles, Part A silicone and Part B catalyzer, respectively. Following chemistry and polymer literature [49], the

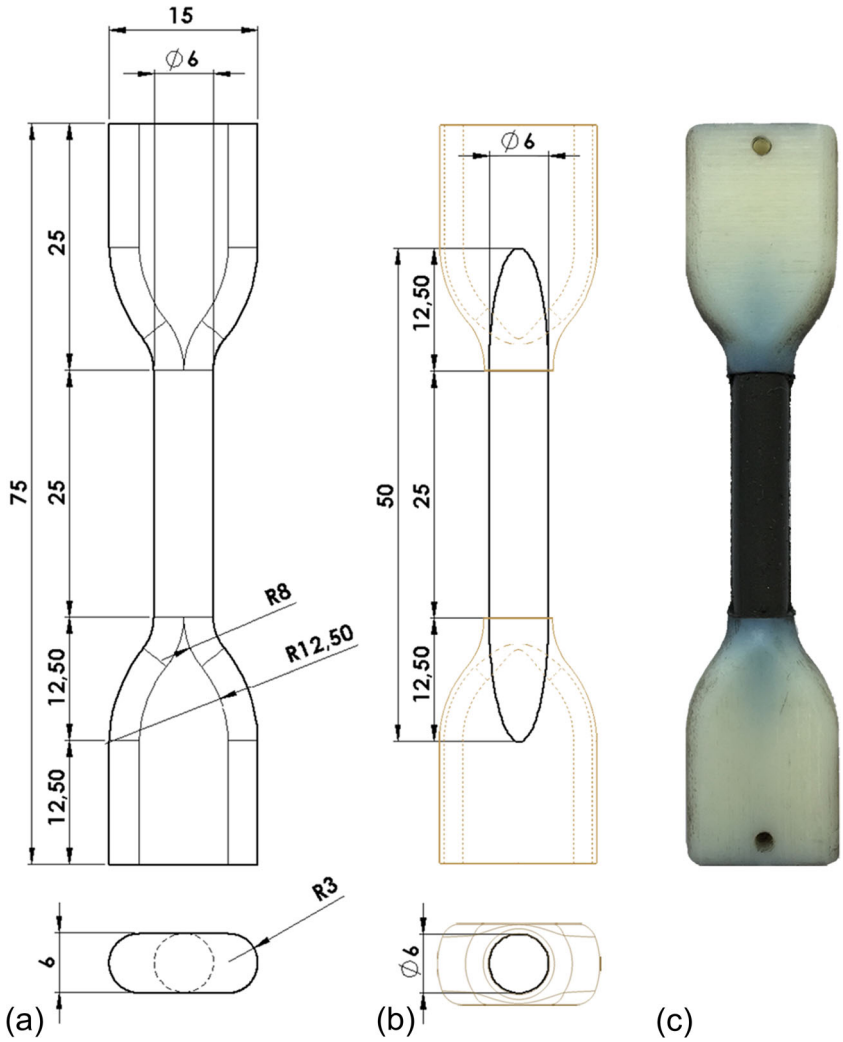

Fig. 2 (**a**) Dimensions (mm) of the fully-MRE dog-bone shape sample with a circular cross-section (**b**) Dimensions (mm) of the sample with a nearly ellipsoidal MRE body and non-magnetic heads (**c**) Picture of the sample with a nearly ellipsoidal MRE body and non-magnetic heads

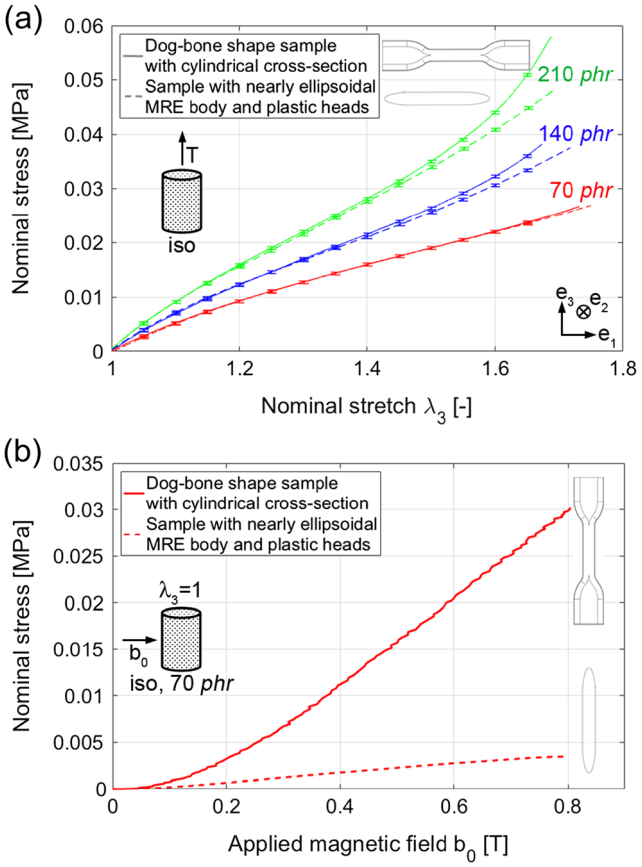

Fig. 3 (**a**) Nominal stress-stretch curve for blends of different particle contents (70, 140 and 210 *phr*) of fully-MRE dog-bone shape samples with a circular cross-section and of samples with a nearly ellipsoidal MRE body and non-magnetic heads (**b**) Stress response of the two aforementioned geometries of 70 *phr* MRE samples held fixed in a uniform magnetic field applied transversely to their longitudinal axis

particle to silicone ratio is henceforth expressed in Parts per Hundred Rubber (*phr*), i.e. mass of filler per hundred parts of raw compounded polymer mass ($phr = m_{CIP} / (m_A + m_B) * 100$). The CIP density ρ_{CIP} actually only comes into play to calculate the corresponding particle volume fraction ϕ as follows:

$$\phi = \frac{\frac{m_{CIP}}{\rho_{CIP}}}{\frac{m_{CIP}}{\rho_{CIP}} + \frac{(m_A + m_B)}{\rho_{sil}}} = \left(1 + \frac{100}{phr}\frac{\rho_{CIP}}{\rho_{sil}}\right)^{-1}. \quad (2)$$

In this study, we refer to our blends in terms of *phr*. Considering ρ_{CIP} = 7874 kg/m^3, blend contents of 70, 140 and 210 *phr* actually correspond to 8.7, 16 and 22.2% volume fractions, respectively.

Even though the quality of the interfacial adhesion between the filler particles and the matrix greatly influences the mechanical behavior of composite materials, especially under large deformations, this topic has rarely been considered in detail in the case of MREs. We previously investigated the interfacial adhesion between the CIP particles and the silicone matrix used in this manuscript for samples of different particle content submitted to a purely mechanical loading [50]. We found that a silane primer treatment of the particles prior to sample fabrication improved the macroscopic mechanical behavior in terms of ultimate load carrying capacity by preventing debonding of the particles from the matrix, though only above a critical stretch threshold that depends on particle content and decreases with it. Hence in the stretch and particle contents targeted in the present work, particle treatment does not influence the mechanical response. Nevertheless, we discovered in this study that the previous results and thresholds, found for MRE samples submitted to purely uniaxial mechanical loadings, do not hold when magnetic loadings are at play. As shown in Fig. 4 for the 210 *phr* blend (the highest particle content has the highest debonding propensity), we consider MRE samples containing uniformly distributed particles that are either treated or untreated (solid lines versus dashed lines). All plots correspond to the upload part of the 3rd stabilized cycle (see details in the *Experimental Methods* section). Under purely mechanical loading, such dog-bone shape samples with cylindrical cross-section exhibit the same nominal stress-nominal stretch response (Fig. 4(a)). However, such samples with a nearly ellipsoidal MRE body and non-magnetic heads, when submitted to a uniform magnetic field perpendicular to their main axis while the force is maintained at 0 N, exhibit different principal stretch ratios for a relatively low applied magnetic field $\mathbf{b}_0$ = 0.2 T while the corresponding stretch values remain well below the stretch threshold found under purely mechanical loading (Fig. 4(b)). The debonding that occurs under the magnetic field can be seen more clearly when looking at the Jacobian of the transformation $J = \det(\lambda_1\ \lambda_2\ \lambda_3)$ in Fig. 4 (c)(d), where λ_1, λ_2, λ_3 are the three principal stretch ratios of the sample. Error bars are included to quantify the error in calculating J from the measured principal stretch ratios. This error is on the order of 8×10^{-4} and confirms that reported values that are slightly below 1 are within experimental error since J cannot theoretically be smaller than 1. In the case of the purely mechanical test (Fig. 4(c)), the Jacobian remains around 1 with a maximum deviation of 0.003 at a 1.6 stretch whether the sample had its particles treated or not, thus confirming that there is very minute to no debonding. However, during the application of a magnetic field on an untreated sample (Fig. 4 (d)), J steadily increases with the magnetic field and already reaches a value of 1.006 for only a 1.05 stretch in the field direction. The reported increase in volume in the untreated case indicates that cavities are created in the MRE when the particles interact with the magnetic field, demonstrating that the debonding between the particles and the matrix is much stronger under magnetic loading than under mechanical loading. As a consequence, only particles used in MRE samples dedicated to coupled magneto-mechanical tests will be pre-treated in this study.

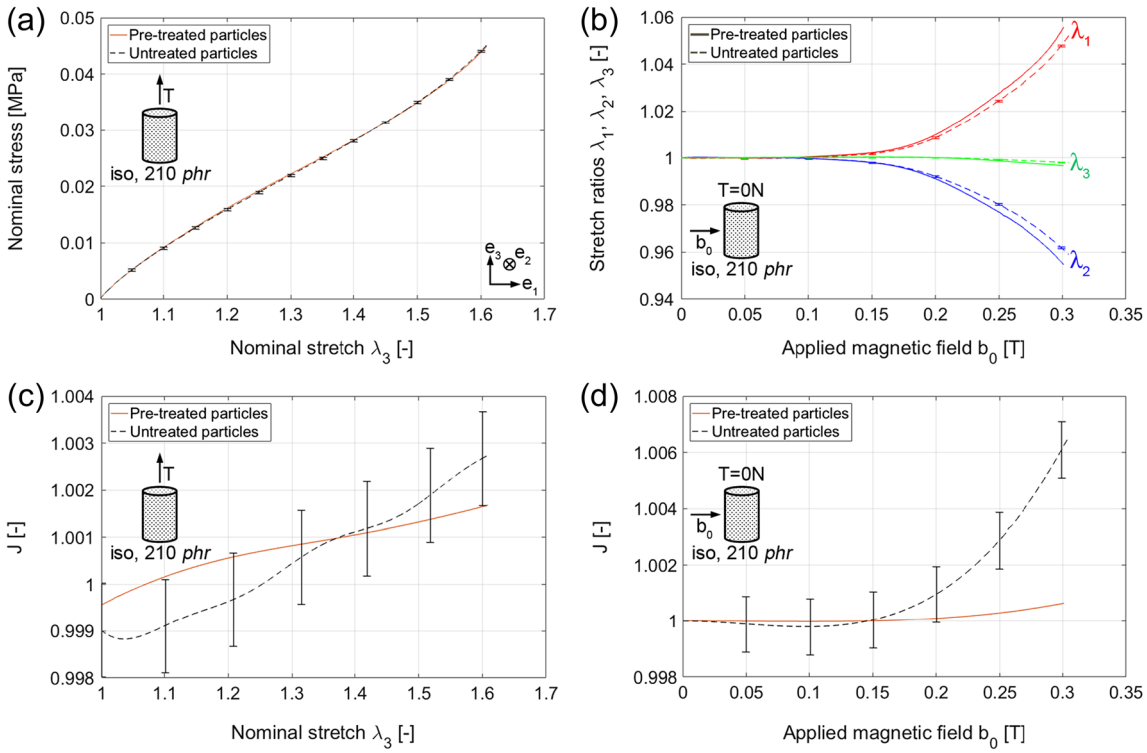

Fig. 4 Comparison of the response of 210 *phr* MRE samples for which particles have been either treated (solid lines) or untreated (dashed lines) (**a**) Mechanical nominal stress-nominal stretch response of such dog-bone shaped samples with a cylindrical cross-section, (**b**) Principal stretch ratios of such samples with a nearly ellipsoidal MRE body and non-magnetic heads subjected to a uniform magnetic field $\mathbf{b}_0$ perpendicular to their main axis while the force is maintained at 0 N (**c**) Jacobian of the transformation during a purely mechanical test on a treated and untreated sample (**d**) Jacobian of the transformation during a magneto-mechanical test on a treated and untreated sample

Fabrication Procedure

Only particles used for MRE samples dedicated to coupled magneto-mechanical tests are pre-treated with a silane primer, vinyltrimethoxysilane 97% from Sigma-Aldrich. Particles are first rinsed: they are soaked in isopropanol and placed in an ultrasonic bath for 2 min. The mix is then filtrated through a 3 to 5 μm porosity mesh. Retained particles are transferred to a beaker filled with vinyltrimethoxysilane and placed in an ultrasonic bath for 4 min. This mix is again filtrated and the retained particles are transferred to a beaker placed on a hot plate set at 60 °C for 1 h to dry before being ready to use in the remainder of the procedure. To fabricate pure silicone material, the elastomer (Part A) and the catalyzer (Part B) are dispensed in a beaker in a 1:1 weight ratio. In the case of MRE samples, the desired mass of particles and the polymer (Part A) are blended and mechanically mixed for 2 min to ensure a proper dispersion of the particles among the polymer molecular chains before starting the polymerization of the network by adding the catalyzer (Part B). This blend is again mixed thoroughly for 3 min. In both cases, the final compound is degassed at 1 bar vacuum for 6 min to eliminate air entrapped during mixing and poured by hand in a mold. Finally, curing is performed by heating the mold up to 100 °C at 10 °C/min, maintaining it at 100 °C for 60 min and letting it cool down to room temperature. Though this silicone can be cured at room temperature within 24 h, accelerating the process via heating has two advantages: it locks particles in place quickly to avoid settling down during curing and it reduces manufacturing time.

In order to fabricate a sample of the desired shape, dedicated molds are machined out of copper for its high thermal conductivity and negligible magnetic susceptibility [46]. For the dog-bone sample with a circular cross-section (Fig. 2(a)), the negative half imprint of the sample is machined out of a pair of plates (each measuring 81 mm × 60 mm × 4.5 mm) forming a mold when assembled together. A detachable piece located next to the sample heads provides clearance to fill the material into the mold along the sample height and is reattached before curing. For the sample with nearly ellipsoidal MRE body and plastic heads (Fig. 2(b)), the negative half imprint of the fully assembled sample is also machined out of a pair of plates (81 mm × 60 mm × 5.5 mm). The lower 3D–printed plastic head is inserted before assembling the mold, the MRE mixture is then poured, the upper 3D–printed plastic head inserted and the mold finally closed. For this sample, the part of the plastic heads in contact with the MRE mixture is coated with a primer (Primer 3 from ACC Silicone) to enhance adhesion between the rigid plastic heads and the soft body of the sample.

To obtain a non-magnetic heating system, each of the above-mentioned molds can be sandwiched between two other copper plates (81 mm × 60 mm × 3 mm) that each bear, at the center of their external surface, a 30 W copper heating resistance covering an area of 76.2 mm × 41.9 mm. A non-magnetic type T thermocouple (0.5 °C precision) is inserted in one half imprint of each mold close to the center of the sample, and connected to a temperature on/off PID regulation system that delivers electric current to the resistance following the desired heating schedule. To fabricate transversely isotropic MRE samples, the mold and its heating system are placed on a stand at the center of a two-coil electromagnet generating a 0.8 T field between two 90 mm-diameter poles separated by an 82 mm-air gap. Different stands thus permit the fabrication of samples having chains of particles of different orientations, namely along the sample longitudinal direction (so that chains are perpendicular to the field during the tests) and along the sample transverse direction (so that chains are either parallel or perpendicular to the field during the tests). When curing is conducted under the magnetic field, the mold is placed within the poles before the magnetic field $\mathbf{b}_0$ is linearly increased from 0 to 0.8 T in 340 s. The curing schedule then starts when the maximum field is attained. Note that raising the magnetic field faster or starting the curing before the maximum field is attained leads to either aggregates in the microstructure or large zones with fewer particles. Hence the above-mentioned parameters need to be tuned and the samples studied under a Scanning Electron Microscope to ensure that the desired microstructure is obtained and can be in a repeatable fashion. Note also that only one sample at a time can be cured since the presence of neighboring MRE samples in the magnetic field would compromise the field uniformity within each sample.

Experimental Methods

General Setup

To study the behavior of MREs under coupled magneto-mechanical loading, a dedicated setup, whose overall schematic is given in Fig. 5(a), was designed. It comprises of an electromagnet that produces a uniform field within an air gap and a tension setup that brings the sample in the field and allows for the application of low rate cyclic tensile loadings while monitoring in-situ mechanical and magnetic quantities. The electromagnet was custom-built by Bouhnik SAS and SigmaPhi. It consists of two current conducting water-cooled copper coils mounted on a C-frame, each bearing in their center a truncated conical iron pole 90 mm in diameter, thus concentrating a nearly uniform field across the 82 mm air gap between the poles without induced heating. The generation of the magnetic field is current-controlled via an analogic entry (precision ±50 mA), yielding a maximum field $\mathbf{b}_0$ = 0.8 T at the center of the air gap at 68 A. The magnetic field $\mathbf{b}_0$ is uniform in the central zone of the air gap for all three directions (±1 mT at ±3 mm from the center). It then increases along $\mathbf{e}_1$ towards the poles as well as decreases in directions $\mathbf{e}_2$ and $\mathbf{e}_3$ away from the center. Symmetric tension is applied to the samples by way of two linear Piezo LEGS motors from PiezoMotor installed in opposition (Fig. 5(b)) and providing a total stroke of 80 mm. These motors are insensitive to magnetic fields and in turn do not disturb it. They are operated in a closed-displacement loop thanks to laser-engraved graduated glass rulers installed on their axes and monitored by optical encoders (Renishaw ATOM miniature encoder system). Once integrated in a LabVIEW (National Instruments) in-house interface program, the whole system provides a resolution of 1 μm and a precision of ±3 μm. Each motor is mounted on an aluminum LCAE-600G load cell from OMEGA. At the end of the motors are attached custom-designed spring-loaded clamps that hold the sample during the test (Fig. 5(b) and Fig. 6(a)). They ensure a constant gripping force on the heads of the samples and prevent slippage during tests. This symmetric tension system is attached to an aluminum plate connected to two cylindrical arms gliding within two dry-friction bearings installed outside of the electromagnet (Fig. 5(a) and Fig. 5(b)). This allows removal of the tension system from the electromagnet for mounting the samples prior to testing. With this tension system, tests can be conducted in displacement-controlled or force-controlled modes.

Mechanical Diagnostics

The overall deformation of the sample is measured in-situ via non-contact video extensometry. A 5 Megapixels F-505B Pike CCD camera equipped with a 0.3× telecentric lens is attached to the gliding ensemble (Fig. 5(b)) and takes images of the sample at a rate of 6.5 fps. With a working distance of 173 mm, the field of view is 16 mm × 20 mm, the resolution is 12 μm/pixel and the depth of field is 8 mm. For telecentric lenses, the magnification remains constant throughout the depth of field [51], hence the out-of-plane movement of the sample due to its change in section during tension does not affect trackings carried out on the sample. Additionally, a mirror making a 45° angle with the CCD array is positioned next to the sample and reflects an image of its side towards the camera (Fig. 6(a)). Hence a single image contains a view of both the front and side of the sample (Fig. 6(b)), allowing access to strains along the three principal directions of the sample (Fig. 6(c)). To obtain the longitudinal sample deformation (along $\mathbf{e}_3$), markers—consisting of black (for pure silicone samples) or white (for MRE samples) paint dots—are deposited 6 mm apart from the center along the vertical axis of the sample prior to testing (Fig. 6(c)). It has been verified that points located farther away yield identical results. To obtain the deformation of the sample along $\mathbf{e}_1$ and $\mathbf{e}_2$, one ensures that there is a sharp change of shade at the interface between

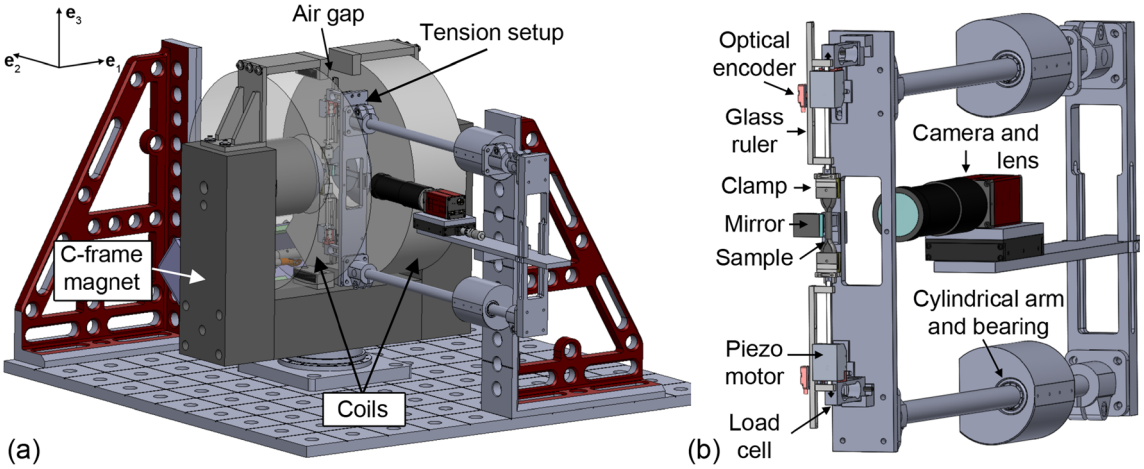

Fig. 5 (**a**) Overall schematic of the magneto-mechanical characterization setup (**b**) Schematic of the symmetric tensile setup showing the motors with their rulers and optical encoders, the load cells, the clamps and the sample. The setup holds a camera for optical diagnostics and can be taken in and out of the electromagnet

the sample and the background. A tracking algorithm implemented in LabVIEW then follows in-situ the two vertical dots and the two pairs of borders, giving access to the overall sample logarithmic strains ε_i along direction $\mathbf{e}_3$, $\mathbf{e}_1$ and $\mathbf{e}_2$, respectively (Fig. 6). The nominal stretch ratios λ_i, corresponding to the variation of length divided by the initial probed length, are obtained via the $\lambda = \exp.(\varepsilon)$ conversion. Note that such macroscopic measurements are equivalent to local ones under purely mechanical tests, which cannot be inferred when the sample deforms under magnetic field unless 3D local strains could be accessed. In fact, very recent numerical work [52] states that, even with nearly uniform magnetization, an MRE sample exhibits local heterogeneities in its mechanical fields. Hence, magnetostriction in the context of MREs refers to an overall sample deformation that may not be representative of the local behavior of the material. The precision on the stretch values is 2×10^{-4} for the dots tracking and 3×10^{-4} for the borders tracking (maximum error found during a rigid body motion were the stretch is expected to remain at unity). The two load cells measuring the force exerted on the sample during loading have a maximum capacity of 6 N and a precision of ±3 mN.

Magnetic Diagnostics

In-situ magnetic field measurements are carried out with transversal Hall probes HGT-2010 from Lakeshore. Their sensitive part is a 760 μm-thick square semi-conductor (2.28 mm × 2.28 mm) mounted at the end of a plastic stem that needs to be strictly perpendicular to the probed field. After calibration against the sensor provided by the electromagnet manufacturer, they yield a precision of ±1% at a

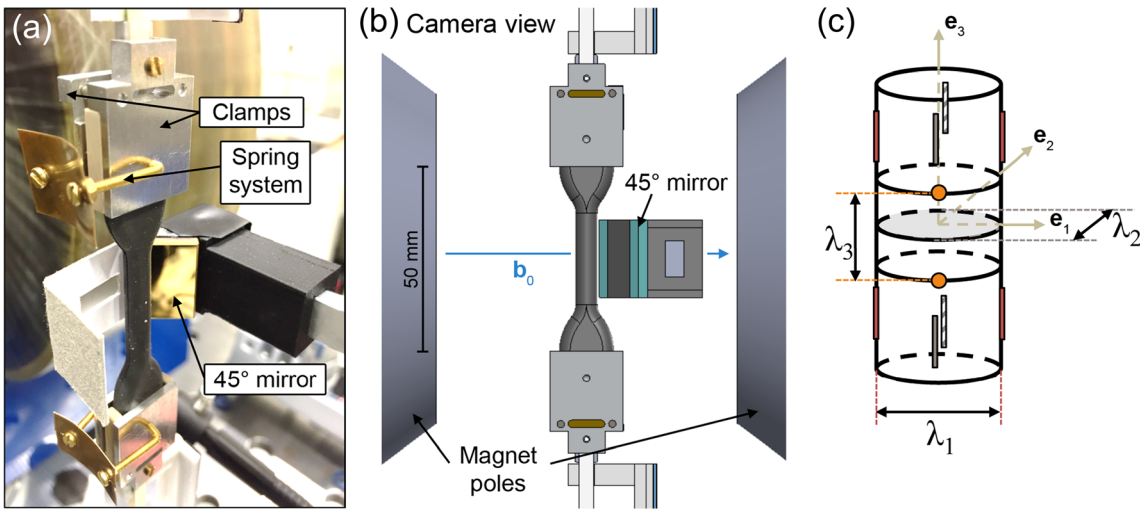

Fig. 6 (**a**) Picture of the setup showing the clamps system holding the specimen and the 45° mirror (**b**) Schematic of the sample held at the center of the electromagnet airgap and of the 45° mirror from the camera vantage point (**c**) Schematic of the dots and borders tracked on the sample and the corresponding principal stretch ratios

range of ±1 T at stable temperature. Thanks to a fixed bracket located behind the electromagnet and equipped with displacement stages (Fig. 7(a)), one probe (probe h) is placed behind the sample in its vertical mid-plane, and can be adjusted along direction $\mathbf{e}_2$. The second probe (probe m) is located on the sample's side so that its center is in the other vertical mid-plane of the sample and can be adjusted along directions $\mathbf{e}_1$ and $\mathbf{e}_2$. Since the samples used for the magnetic measurements have a nearly ellipsoidal MRE body (that remains nearly ellipsoidal in the range of considered deformation), all Eulerian magnetic quantities i.e. the perturbation field $\mathbf{h}_1$ and the magnetization $\mathbf{m}$ (and hence the total magnetic field **b)** are nearly uniform within the sample. Due to the continuity of the tangential component of $\mathbf{h}$ at the interface between the air and the sample, the Hall probe h placed at the back of the sample gives access to the total field $\mu_0\,\mathbf{h}$ [T] inside the material (the externally applied field $\mathbf{h}_0$ plus the perturbation field $\mathbf{h}_1$ measured in air) since the contribution of the magnetization $\mathbf{m}$ vanishes at that point. From the continuity of the normal component of $\mathbf{b}$ at the interface between the air and the sample, the total magnetic field $\mathbf{b}$ [T] inside the sample—now including the contribution of the total $\mathbf{h}$-field (measured at the back) plus the contribution of the magnetization $\mathbf{m}$—is measured by the lateral Hall probe m, allowing access to the magnetization $\mathbf{m}$ inside the sample. The distribution of the magnetic field $\mathbf{b}$ in the airgap in the presence of a magnetic sample is sketched in Fig. 7(b) along with the positions of the h and m sensors.

Prior to the test, with the help of the camera, both probes are positioned to come nearly in contact with the sample but not exactly at the discontinuity interface between the air and the sample due to geometrical limitations. Additionally, the magnetic quantities need to be measured in-situ as the sample deforms and moves away from the sensors. Hence measurements need to be corrected to account for the distance between the sensitive part of the probes and the sample/air interface. Fortunately, the evolution of the $\mathbf{e}_1$ component of both $\mathbf{h}$ and $\mathbf{b}$ along direction $\mathbf{e}_2$ and along direction $\mathbf{e}_1$, respectively, can be derived analytically (this correction is detailed in Online Resource 1). The obtained results are plotted in Fig. 7(c), where the top curve corresponds to the evolution of the $\mathbf{e}_1$ component of the $\mathbf{h}$ field along $\mathbf{e}_2$ and the bottom one to the evolution of the $\mathbf{e}_1$ component of the $\mathbf{b}$ field along $\mathbf{e}_1$, with both curves covering the discontinuity interface between the air and the sample. To link the current value measured away from the sample to the actual value at the sample/air interface, the distance between the sensitive part of the probes and the sample/air interface is monitored in-situ with the borders detection algorithm described earlier.

Testing Protocol

For all tests, a virgin sample is installed and aligned in the tensile setup with the help of the camera as the system is drawn out of the electromagnet. Once the clamps are in place,

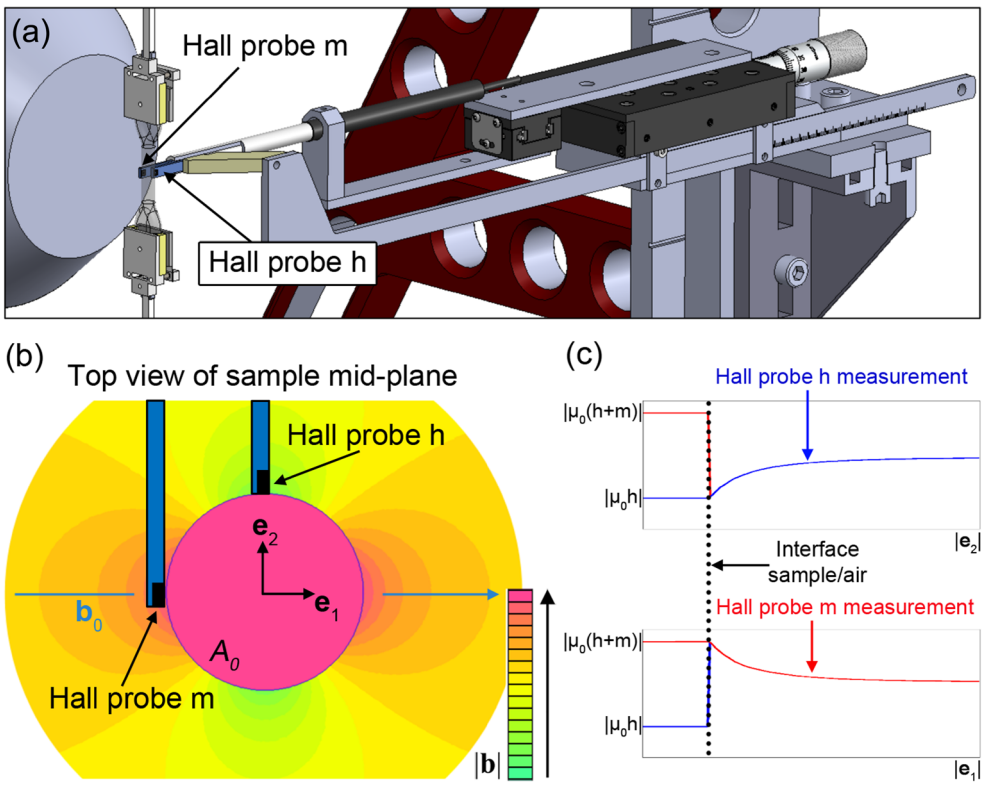

Fig. 7 (**a**) Stand coming from behind the electromagnet and holding the two Hall probes h and m (**b**) 2D plane FEM simulation of the distribution of the magnetic field $\mathbf{b}$ in the airgap of an electromagnet in the presence of a magnetic sample of circular cross-section having a uniform magnetization $\mathbf{m}$. View from top within the horizontal mid-plane of the sample (**c**) Evolution of the $\mathbf{e}_1$ component of the magnetic field $\mathbf{h}$ along $\mathbf{e}_2$ (top) and of the $\mathbf{e}_1$ component of the magnetic field $\mathbf{b}$ along $\mathbf{e}_1$ (bottom). Both curves cover the discontinuity interface between the air and the sample

the setup is glided back inside the electromagnet and the sample lies at the center of the magnet as the applied force and strains equal zero. In the case of purely mechanical tests, the sample is first submitted to cyclic loading prior to the actual test (pre-conditioning) to attain a stabilized behavior after the initial Mullins softening. The pre-cycling (10 cycles) is conducted in displacement-controlled mode between 0 and 30 mm following a sinusoid at a frequency of 0.01 Hz. Following the pre-conditioning, since the sample carries some residual strain, a relaxation time of 10 min is allowed before the motors are displaced to get the sample straight while maintaining the force at 0 N. At this moment, the initial cross-section $A_0 = L_1\ L_2\ \pi/4$ is determined with the help of the camera, where L_1 and L_2 are the lengths of the sample in directions $\mathbf{e}_1$ and $\mathbf{e}_2$ in the gage area, respectively. The nominal stress is obtained by dividing the measured force by this initial cross-section A_0. The actual cyclic test (3 cycles) is then conducted in displacement-controlled mode between 0 and 30 mm following a triangle at a frequency of 0.001 Hz. In the case of the magneto-mechanical tests, either the force or the displacement can be set and maintained at a given value during the test. In this case, the initial state of the sample corresponds to its state after the application of the applied pre-stress or pre-stretch. Since the magnetic field leads to deformations within the sample, Mullins effect can be expected. Hence a pre-conditioning is also conducted. The magnetic field $\mathbf{b}_0$ is thus cycled between 0 and a fixed value so as to perform 10 sinusoidal pre-cycles at a frequency of 0.001 Hz followed by a relaxation time of 10 min and finally 3 triangular test cycles at a frequency of 0.001 Hz.

Results and Discussion

Purely Mechanical Testing

In Fig. 8(a), we first plot the nominal stress-stretch curve of the whole test (10 pre-conditioning cycles and 3 test cycles) for isotropic samples with varying particle contents of 0, 70, 140 and 210 *phr*. The responses of the 140 and 210 *phr* MREs clearly show an initial softening (Mullins effect) while the 70 *phr* sample shows little softening and the pure silicone shows none. Since the first 10 pre-conditioning cycles are carried out at a higher frequency, the data is noisier. Hence for better clarity, only the 3 test cycles carried out at lower frequency are plotted in Fig. 8(b). The stiffness of the MRE increases with particle content since the rigidity of the fillers is much higher than that of the matrix. The same trend is observed for the stabilized hysteresis loops since higher particle content leads to more dissipation due to more friction and rearrangements between the particles and the host matrix. Such results are classically observed in filled elastomers [32].

We now plot in Fig. 9 the mechanical response obtained during the third test cycle (stabilized cycle) for 70 *phr* samples that are either isotropic or field-structured in directions $\mathbf{e}_1$, $\mathbf{e}_2$ and $\mathbf{e}_3$. The minimum stiffness is obtained for the isotropic sample and the maximum stiffness is obtained for the sample having particle chains in the loading direction. Samples having chains in either $\mathbf{e}_1$ or $\mathbf{e}_2$ direction exhibit an intermediate stiffness that is identical since the orientation of their microstructure is the same from a mechanical standpoint. Such behavior is typically observed in fiber-reinforced composites [53]. However, if the increase in stiffness is due to the higher load-bearing capacity of the fibers in the latter, a different mechanism is at play in field-structured MREs, where particle chains are not continuous like fibers. In this case, it is instead friction arising at the microscopic level that leads to the observed increase in stiffness and it is when particles form columns in the loading direction that they impinge the most on polymer chain motion in the loading direction, preventing them from unwinding freely and leading to a higher hysteresis.

Coupled Magneto-Mechanical Testing

Magneto-mechanical tests are first performed on 70 *phr* samples exhibiting different microstructures. The force is maintained at 0 N to impose traction free boundary conditions, thus simulating a sample hanging free in a uniform magnetic field. The applied field $\mathbf{b}_0$ varies between 0 and 0.8 T during 10 pre-conditioning cycles followed by 3 cycles at 0.001 Hz. In the case of the sample field-structured along $\mathbf{e}_3$, a macroscopic instability occurs at $\mathbf{b}_0 = 120$ mT, causing the sample to bend in the direction of the applied field (see Online Resource 2 movie). This instability is comparable to that of an elongated body subjected to a magnetic field transverse to its long axis, and is known as the compass effect [54] (though here the role of the elongated body is played by particles chains). Similarly, for the sample field-structured along $\mathbf{e}_2$, the compass effect yields a rotation of the body of the sample about $\mathbf{e}_3$. The rotation angle increases with the magnetic field to attain 90° at $\mathbf{b}_0 = 99$ mT and remains stable thereafter (see Online Resource 3 movie). The whole test mentioned above can be carried out without occurrence of instability on 70 *phr* samples that are either isotropic or field-structured along $\mathbf{e}_1$. Numerical investigations in idealized multilayered composite structures simulating field-structured MREs [55] confirm our findings regarding either the occurrence or the absence of macroscopic instabilitiy in $\mathbf{e}_3$ and $\mathbf{e}_1$ field-structured samples, respectively. In the reported simulations, it is found that the magnetic field promotes instabilities when perpendicular to the particle chains whereas it stabilizes the sample when parallel to the particle chains. In the latter case, we can assume that because the particle chains are already aligned along the magnetic field, little to no compass effect can arise before

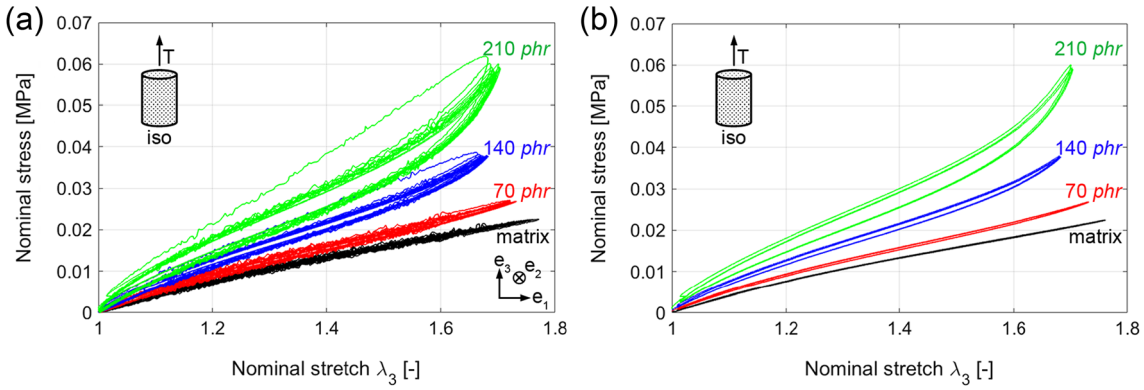

Fig. 8 Nominal stress-stretch curves obtained during purely mechanical tensile tests on isotropic samples with varying particle contents of 0, 70, 140 and 210 *phr* (**a**) Curves obtained over the whole test (10 pre-conditioning cycles and 3 test cycles) (**b**) Curves obtained during the 3 test cycles

magnetic saturation is attained in the samples, thus leaving them free of macroscopic instabilities.

Thus we can now compare the principal stretch ratios of an isotropic sample (Fig. 10(a)) with those of an $\mathbf{e}_1$ field-structured sample (Fig. 10(b)) during the 3rd stabilized cycle.

In the isotropic case, the largest stretch is an elongation along the field direction $\mathbf{e}_1$ and is accompanied with contractions in the other two transverse directions, leading to a transformation of the originally circular cross-section into a quasi-elliptic one. These deformations are macroscopic manifestations of the particle motions as they try to align along the lines of the magnetic field. Even though $\mathbf{e}_2$ and $\mathbf{e}_3$ are equivalent orientations relative to the magnetic field, the sample contracts more along $\mathbf{e}_2$ than $\mathbf{e}_3$. Here it is important to note that despite a uniform magnetic field within the sample, its overall response is affected by a shape effect: the perturbation field $\mathbf{h}_1$ is indeed related to the uniform magnetization $\mathbf{m}$ through $\mathbf{h}_1 = -\mathrm{D}\,\mathbf{m}$, where the demagnetizing factor D depends on the shape [20, 38]. This factor is smaller in the ($\mathbf{e}_1$, $\mathbf{e}_3$) plane due to a higher aspect ratio, yielding a smaller

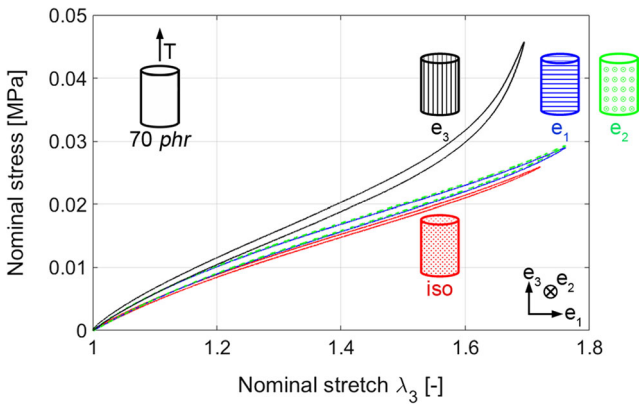

Fig. 9 Stabilized stress-stretch curve obtained during purely mechanical tensile tests on 70 *phr* samples with different microstructures: isotropic or field-structured in directions $\mathbf{e}_1$, $\mathbf{e}_2$ and $\mathbf{e}_3$

magnetostriction (field-induced macroscopic sample deformation). The sample field-structured along $\mathbf{e}_1$ exhibits its largest deformation as a contraction along direction $\mathbf{e}_2$ while it shows small elongations in the field direction $\mathbf{e}_1$ and along $\mathbf{e}_3$. All these deformations remain very small (<0.7%) even at saturation. It actually seems that the particles have already attained a stable equilibrium position during sample curing and that these strains are due to the fact that, even though the relative orientation sample/field is the same, the absolute orientation is different during curing. These experimental observations are similar to what has been observed for cylindrical samples whose main axis is aligned along the magnetic field [20, 37, 56], i.e. we report elongation in the direction of the applied field and a larger magnetostriction for isotropic samples. In particular, at 0.8 T, the magnetostriction is 10.6% in the field direction for isotropic samples and only 0.7% for samples field-structured in the magnetic field direction.

In parallel, it is interesting to look at the magnetization curves of these samples (Fig. 10(c)) in which the bottom parts of the loops are obtained while the magnetic field increases, as is the case in classical magnetization curves of ferromagnetic bulk materials. The $\mathbf{e}_1$ field-structured sample magnetizes itself much faster than the isotropic sample and attains saturation, whereas the isotropic samples does not. We interpret this as follows: the $\mathbf{e}_1$ field-structured sample magnetizes and saturates fast because the small amount of motion among its particles leads to an early stabilization. For the isotropic sample, magnetization is slower, hence the overall composite is less susceptible because the particles keep moving locally throughout the increase of the magnetic field in order to keep minimizing the energy of the whole sample as it deforms. As a result, samples for which the microstructure interacts weakly with the magnetic field (because they are already in an optimal state in regards to the field) exhibit a higher initial susceptibility and a faster saturation. On the contrary, samples that interact the most with the magnetic field (because the particles need significant rearrangement to reach an optimal state) exhibit a lower initial

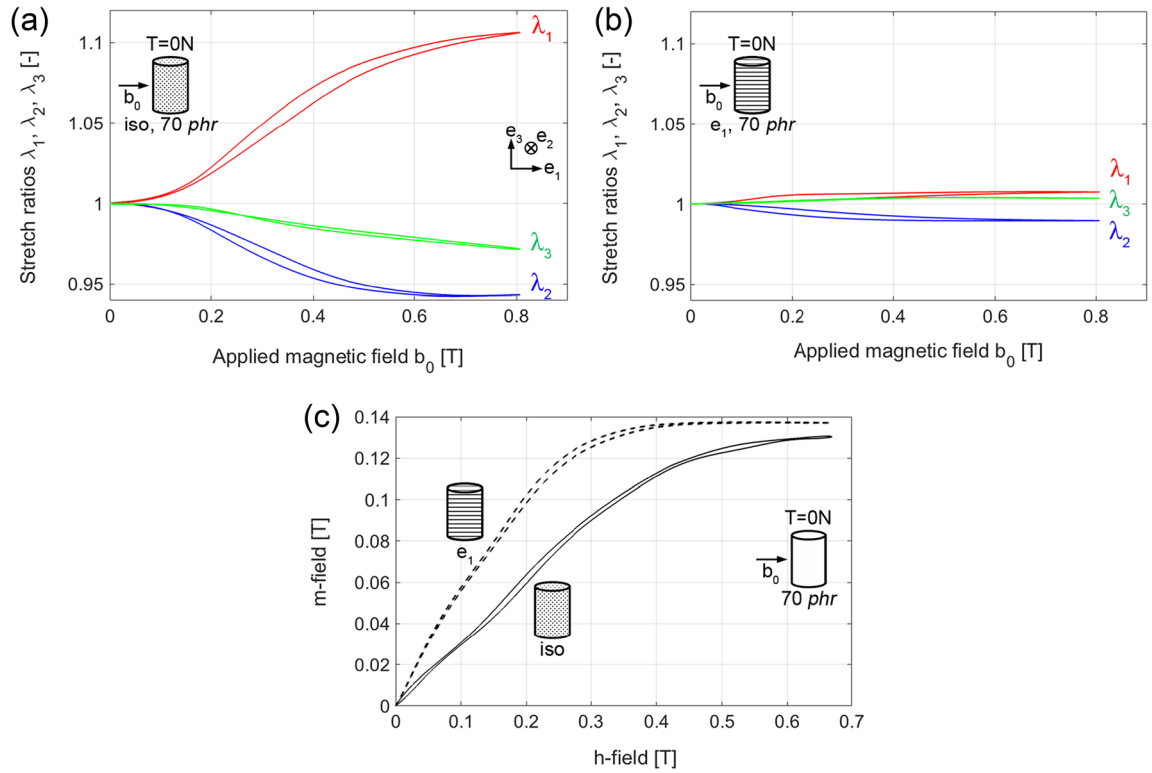

Fig. 10 Response as a function of the applied magnetic field $\mathbf{b}_0$ obtained during the 3rd stabilized cycled for 70 *phr* samples exhibiting different microstructures and submitted to a coupled magneto-mechanical test as the force is maintained at 0 N (**a**) Principal stretch ratios for the isotropic sample (**b**) Principal stretch ratios for the sample field-structured along $\mathbf{e}_1$ (**c**) Magnetization curves for both samples

susceptibility. However, the microstructure is rearranged to correct this and in turn delays the saturation in the sample. Finally, for our samples, both the stretch and the magnetization go readily back to their initial value when the magnetic field vanishes. The latter observation indicates that the MRE composite, whose fillers do not have remanent magnetization, does not exhibit any remanent magnetization either. The former observation actually only shows that there is no residual stretch induced by particle debonding. In the case of samples with untreated particles (not shown here for the sake of brevity), the magnetization also goes back to zero but the samples exhibit residual strains as the applied magnetic field vanishes. This confirms that the observed residual strains are not linked to remanence as initially suggested [37], but to mechanical phenomena arising within the samples and in particular to the debonding that is demonstrated here to play an important role in the MREs response during coupled tests.

Since the isotropic sample exhibits the highest magnetostriction, the effect of particle content is only studied on such samples. However the magneto-mechanical test in which the force is maintained at 0 N suffers an instability arising at lower magnetic field as particle content increases from 70 *phr* (0.45 T for 140 *phr*, 0.3 T for 210 *phr*). The sample starts to deform similarly to the 70 *phr* sample but eventually tries to align along the magnetic field similarly to the $\mathbf{e}_3$ field-structured sample. In fact, the instability occuring in isotropic samples, for which the field direction is perpendicular to the sample's long axis, has been investigated theoretically but mainly in the idealized case of a rectangular block in plane strain [57]. Instability arises at a critical magnetic field reported to increase monotonically with the aspect ratio of the sample. Very recent numerical investigations in idealized periodic composite structures simulating isotropic MREs [42] also report that instabilities in such samples occur at lower magnetic field as the particle content increases, as observed in our experiments. In our case, since the sample aspect ratio is high (8.3), the risk of occurrence of instability is already lowered. Nevertheless, the influence of particle content on magnetostriction can still be studied since the reported instabilities are delayed, even avoided, when a sufficient pre-stress or pre-stretch is applied to the samples so as to increase their aspect ratio. In order for particle content to be the only varying parameter, the same pre-stretch needs to be imposed to all samples so that they have the same aspect ratio when the coupled test starts. To select the maximum pre-stretch applicable to all samples while ensuring that their mechanical response is representative of the material, we refer to Fig. 3(a) that gives, for each particle content, the maximum stretch (1.4) for which there is no debonding at the plastic heads/MRE body interface. From this, the maximum magnetic field that can be prescribed without triggering an

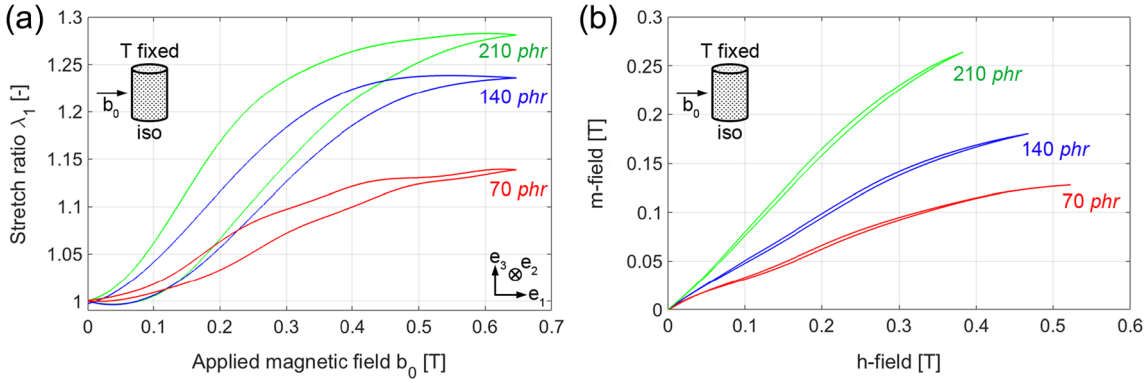

Fig. 11 Magneto-mechanical tests on 70 *phr*, 140 *phr* and 210 *phr* isotropic samples. After application of a 1.4 pre-stretch, the corresponding force remained fixed throughout the tests (**a**) Stretch in the field direction as a function of the applied magnetic field $\mathbf{b}_0$ during the 3rd stabilized cycle (the reference configuration is taken post pre-stretch) (**b**) Magnetization curves obtained during the 3rd stabilized cycle

instability must be determined for an isotropic sample of highest particle content submitted to a pre-stretch of 1.4, given here as 0.65 T. Finally, magneto-mechanical tests (including pre-conditioning and cycling) up to 0.65 T can be carried out on 70 *phr*, 140 *phr* and 210 *phr* isotropic samples that are initially submitted to a 1.4 pre-stretch and for which the corresponding force remains fixed throughout the rest of the test. The evolution of the stretch ratio in the field direction (λ_1) as a function of the applied magnetic field $\mathbf{b}_0$ during the 3rd stabilized cycle is plotted in Fig. 11(a) for isotropic samples of 70 *phr*, 140 *phr* and 210 *phr*. Note that the state of the sample after the application of the 1.4 pre-stretch is considered as the reference configuration (the plotted λ_1 thus start from unity). For all tested samples, the λ_1 stretch ratio evolution describes a hysteresis loop whose area increases slightly with particle content. The maximum amplitude of stretch is attained for the highest particle content, but the value of the maximum stretch does not increase linearly with particle content. In fact, beyond a given particle content (known as "optimal filling factor" [7, 20, 58]), increasing it further would not lead to more magnetostriction as the composite would become too stiff. The magnetization curves obtained during these tests are plotted in Fig. 11(b). The initial slope or magnetic susceptibility increases with particle volume fraction but these curves do not reach saturation since the ideal stabilized state of the sample would happen post-instability. These experimental results may thus shed some light on the macroscopic instability mechanism. As the magnetic field increases, particles first rearrange themselves to align along the lines of the magnetic field. If saturation is reached at the maximum applied magnetic field, only magnetostriction is observed. However if the sample is still far away from saturation, beyond the microscopic rearrangement of the particles, a macrospic realignment of the whole sample through the compass effect is needed to reach its ideal stabilized state in regard of the applied magnetic field (that is perpendicular to the sample). Hence, because saturation increases with particle content, the macroscopic instability in isotropic samples happens at lower magnetic field in samples with higher particle content.

A final aspect of interest that can be clarified due to our specially designed setup and samples is the effect of a pre-stress on the magnetic behavior of MREs. It was recently suggested [59] that MREs might exhibit a change in their magnetic susceptibility when subjected to a mechanical stress (Villari effect or inverse magnetostrictive effect). The reported experimental results indeed showed a little sensitivity but the involved samples did not have their particles pre-treated. In order to investigate experimentally the effect of pre-stress, which was predicted numerically to have no effect on the magnetization [29], a 70 *phr* isotropic sample was submitted to a full coupled test as the force was maintained at different values: 0 N, 0.1 N and 0.2 N. The corresponding magnetization curves obtained during the 3rd stabilized cycle are plotted in Fig. 12 and confirm that pre-stress does not influence the magnetic response of the sample.

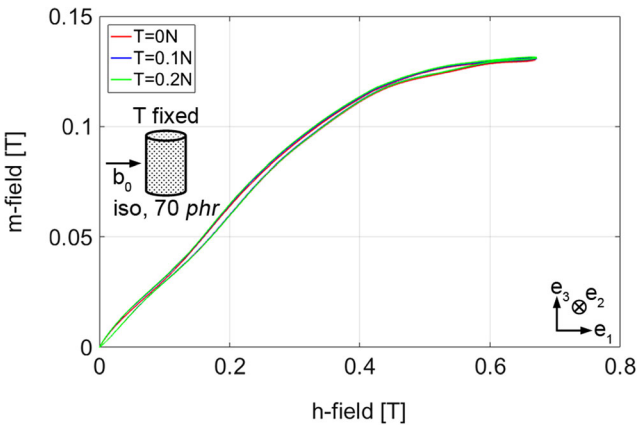

Fig. 12 Magnetization curves obtained during the 3rd stabilized cycle for a 70 *phr* isotropic sample submitted to a coupled test as the force is maintained at 0 N, 0.1 N and 0.2 N

Conclusions

The present study introduces an experimental setup enabling the measurement, in-situ and with precision, of both the magnetic state and the macroscopic deformation of a dedicated MRE sample, in which nearly uniform magnetization is achieved. This investigation of MREs is conducted from the perspective of the mechanics of filled polymers to ensure reliability and repeatability of the results. In particular, MRE samples are systematically pre-conditioned to prevent the Mullins effect from impinging on the results. It is found that debonding between the particles and the matrix, though less of an issue under purely mechanical tests, can lead to significant volume change during magnetic tests and render false the incompressibility assumption if ignored. Hence the preparation of MRE samples is crucial. It involves not only the pre-treatment of the particles but also a careful study of the obtained microstructures according to the curing schedule and the rate of application of the magnetic field. The conducted experiments highlight that instabilities are ubiquitous in MREs. Hence low power applications may benefit greatly from these instabilities if properly harnessed. The experiments demonstrate, however, that pre-stretching the samples before testing can minimize macroscopic instabilities due to the compass effect. Tests carried out on MRE samples of various microstructures show that the only samples remaining macroscopically stable during the experiments are the isotropic ones (possibly with pre-stretch) and the ones that are field-structured in the direction of the applied field. In fact, the field-structured samples experience little magnetostriction when submitted to a magnetic field similar to the one applied during fabrication. Only the isotropic samples exhibit significant magnetostriction along the direction of the applied field. Results for these samples also show that the maximal magnetostriction increases with particle content. Nevertheless, the rate of increase is not linear and tends to saturate as the amount of filler stiffens the matrix. It is also observed that the magnetization response of the sample is independent of the pre-stress applied on the sample prior to testing. Such experimental results may provide useful data for the assessment of magneto-mechanical models dedicated to MREs that rely, for validation purposes, on a near uniform magnetic field within the modeled sample. Here it is important to note that since three-dimensional mechanical fields induced in the sample by the magnetic field cannot be accessed, they cannot be assumed uniform, and moreso in light of recent numerical results [50]. Additionally, as seen in the results, since shape effects (demagnetizing factor and macroscopic instabilities) remain intrinsically present in the sample, any attempt to derive constitutive models for MREs will need to account for all structural effects arising in MREs through a strong experimental-numerical dialog. Further experimental developments include significantly modifying the setup to permit the application of the magnetic field along the main axis of the sample; studying the optimal filling factor for varying matrix materials; and, in the long term, accessing local mechanicals fields by X-ray tomography.

Acknowledgements The authors acknowledge LMS engineers Vincent De Greef for tailoring the acquisition software to the magneto-mechanical experiments, Erik Guimbretière for his contribution to the setup design as well as François Lelong and Antoine Soler for machining. We also thank Kostas Danas and Nick Triantafyllidis for their help on theoretical and numerical aspects. The contribution of Lingjie Cai during his master internship is also acknowledged.

References

1. Hamrock B (2006) Mechanical Engineers' Handbook: Materials and Mechanical Design. Wiley, Columbus
2. Rigbi Z, Jilken L (1983) The response of an elastomer filled with soft ferrite to mechanical and magnetic influences. J Magn Magn Mater 37:267–276. https://doi.org/10.1016/0304-8853(83)90055-0
3. Bustamante R (2007) Mathematical modelling of non-linear magneto-and electro-active rubber-like materials. Dissertation, University of Glasgow
4. Farshad M, Benine A (2004) Magnetoactive elastomer composites. Polym Test 23:347–353. https://doi.org/10.1016/S0142-9418(03)00103-X
5. Gong X, Zhang X, Zhang P (2005) Fabrication and characterization of isotropic magnetorheological elastomers. Polym Test 24:669–676. https://doi.org/10.1016/j.polymertesting.2005.03.015
6. Chen L, Gong X, Jiang W, Yao J, Deng H, Li W (2007) Investigation on magnetorheological elastomers based on natural rubber. J Mater Sci 42:5483–5489. https://doi.org/10.1007/s10853-006-0975-x
7. Kallio M (2005) The elastic and damping properties of magnetorheological elastomers. Dissertation, VTT Technical Research Centre of Finland
8. Gong X, Chen L, Li J (2007) Study of utilizable magnetorheological elastomers. Int J M P B 21:4875–4882. https://doi.org/10.1142/S0217979207045785
9. Carlson JD, Jolly MR (2000) MR fluid, foam and elastomer devices. Mechatronics 10:555–569. https://doi.org/10.1016/S0957-4158(99)00064-1
10. Jolly MR, Carlson JD, Muñoz BC, Bullions TA (1996) The magnetoviscoelastic response of elastomer composites consisting of ferrous particles embedded in a polymer matrix. J Intell Mater Syst Struct 7:613–622. https://doi.org/10.1177/1045389X9600700601
11. Ginder JM, Nichols ME, Elie LD, Clark SM (2000) Controllable-stiffness components based on magnetorheological elastomers. SPIE's 7th Annual International Symposium on Smart Structures and Materials. https://doi.org/10.1117/12.388844
12. Lokander M, Stenberg B (2003) Performance of isotropic magnetorheological rubber materials. Polym Test 22:245–251. https://doi.org/10.1016/S0142-9418(02)00043-0
13. Elie L, Ginder J, Nichols M, Stewart W (2002) Variable stiffness bushing using magnetorheological elastomers. European Patent
14. Farshad M, Le Roux M (2004) A new active noise abatement barrier system. Polym Test 23:855–860. https://doi.org/10.1016/j.polymertesting.2004.02.003
15. Crist RJ (2009) Active vibrational damper. United States Patent
16. Marur PR (2013) Magneto-rheological elastomer-based vehicle suspension. United States Patent Application Publication

17. Kim MS, Yang KM, Lee SH, Yoon JH, Jeong UC, Yang IH, Oh JE (2014) Variable differential mount apparatus using magnetorheological elastomer. United States Patent
18. Thorsteinsson F, Gudmundsson I, Lecomte C (2015) Prosthetic and orthotic devices having magnetorheological elastomer spring with controllable stiffness. United States Patent Application Publication
19. Diguet G, Beaugnon E, Cavaillé J (2009) From dipolar interactions of a random distribution of ferromagnetic particles to magnetostriction. J Magn Magn Mater 321:396–401. https://doi.org/10.1016/j.jmmm.2008.08.112
20. Diguet G, Beaugnon E, Cavaillé J (2010) Shape effect in the magnetostriction of ferromagnetic composite. J Magn Magn Mater 322: 3337–3341. https://doi.org/10.1016/j.jmmm.2010.06.020
21. Shen Y, Golnaraghi MF, Heppler G (2004) Experimental research and modeling of magnetorheological elastomers. J Intell Mater Syst Struct 15:27–35. https://doi.org/10.1177/1045389X04039264
22. Martin JE, Anderson RA, Read D, Gulley G (2006) Magnetostriction of field-structured magnetoelastomers. Phys Rev E 74:051507. https://doi.org/10.1103/PhysRevE.74.051507
23. Schubert G, Harrison P (2015) Large-strain behaviour of Magneto-Rheological Elastomers tested under uniaxial compression and tension, and pure shear deformations. Polym Test 42:122–134. https://doi.org/10.1016/j.polymertesting.2015.01.008
24. Schubert G, Harrison P (2016) Equi-biaxial tension tests on magneto-rheological elastomers. Smart Mater Struct 25:015015. https://doi.org/10.1088/0964-1726/25/1/015015
25. Bossis G, Abbo C, Cutillas S, Lacis S, Métayer C (2001) Electroactive and electrostructured elastomers. Int J M P B 15: 564–573. https://doi.org/10.1142/S0217979201005027
26. Bellan C, Bossis G (2002) Field dependence of viscoelastic properties of MR elastomers. Int J M P B 16:2447–2453. https://doi.org/10.1142/S0217979202012499
27. Coquelle E, Bossis G (2005) Magnetostriction and piezoresistivity in elastomers filled with magnetic particles. J Adv Sci 17:132–138. https://doi.org/10.2978/jsas.17.132
28. Kankanala SV (2007) On finitely strained magnetoelastic solids. Dissertation, University of Michigan
29. Danas K, Kankanala S, Triantafyllidis N (2012) Experiments and modeling of iron-particle-filled magnetorheological elastomers. J Mech Phys Solids 60:120–138. https://doi.org/10.1016/j.jmps.2011.09.006
30. Mullins L (1948) Effect of stretching on the properties of rubber. Rubber Chem Technol 21:281–300. https://doi.org/10.5254/1.3546914
31. Mullins L, Tobin N (1957) Theoretical model for the elastic behavior of filler-reinforced vulcanized rubbers. Rubber Chem Technol 30:555–571. https://doi.org/10.5254/1.3542705
32. Miehe C, Keck J (2000) Superimposed finite elastic-viscoelastic-plastoelastic stress response with damage in filled rubbery polymers. Experiments, modelling and algorithmic implementation. J Mech Phys Solids 48:323–365. https://doi.org/10.1016/S0022-5096(99)00017-4
33. Coquelle E, Bossis G (2006) Mullins effect in elastomers filled with particles aligned by a magnetic field. Int J Solids Struct 43:7659–7672. https://doi.org/10.1016/j.ijsolstr.2006.03.020
34. Dekkers M, Heikens D (1983) The effect of interfacial adhesion on the tensile behavior of polystyrene-glass-bead composites. J Appl Polym Sci 28:3809–3815. https://doi.org/10.1002/app.1983.070281220
35. Gent A, Park B (1984) Failure processes in elastomers at or near a rigid spherical inclusion. J Mater Sci 19:1947–1956. https://doi.org/10.1007/BF00550265
36. Fu S, Feng X, Lauke B, Mai Y (2008) Effects of particle size, particle/matrix interface adhesion and particle loading on mechanical properties of particulate-polymer composites. Compos Eng 39: 933–961. https://doi.org/10.1016/j.compositesb.2008.01.002
37. Guan X, Dong X, Ou J (2008) Magnetostrictive effect of magnetorheological elastomer. J Magn Magn Mater 320:158–163. https://doi.org/10.1016/j.jmmm.2007.05.043
38. Osborn J (1945) Demagnetizing factors of the general ellipsoid. Phys Rev 67:351. https://doi.org/10.1103/PhysRev.67.351
39. ASTM Standard D412-06 (2006) Standard Test Methods for Vulcanized Rubber and Thermoplastic Elastomers-Tension. ASTM International, West Conshohocken. https://doi.org/10.1520/D0412-06
40. ISO 37:2011 (2011) Rubber, vulcanized or thermoplastic - Determination of tensile stress-strain properties. International Organization for Standardization, Geneva, Switzerland
41. Galipeau E, Rudykh S, deBotton G, Ponte Castañeda P (2014) Magnetoactive elastomers with periodic and random microstructures. Int J Solids Struct 51:3012–3024. https://doi.org/10.1016/j.ijsolstr.2014.04.013
42. Goshkoderia A, Rudykh S (2017) Stability of magnetoactive composites with periodic microstructures undergoing finite strains in the presence of a magnetic field. Compos Eng 128:19–29. https://doi.org/10.1016/j.compositesb.2017.06.014
43. ASTM E8-01 (2001) Standard test methods for tension testing of metallic materials. ASTM International, West Conshohocken. https://doi.org/10.1520/E0008-01
44. ISO 6892-1:2016 (2016) Metallic materials Tensile testing Part 1: Method of test at room temperature. International Organization for Standardization, Geneva, Switzerland
45. Brown W (1962) Magnetostatic Principles. North-Holland Publishing Company, Amsterdam
46. Haynes WM (2014) CRC handbook of chemistry and physics. CRC press, Boca Raton
47. Schubert G (2014) Manufacture, characterisation and modelling of magneto-rheological elastomers. Dissertation, University of Glasgow
48. Gorodkin S, James R, Kordonski W (2009) Magnetic properties of carbonyl iron particles in magnetorheological fluids. J Phys Conf Ser 149. https://doi.org/10.1088/1742-6596/149/1/012051
49. Ciesielski A (1999) An introduction to rubber technology. iSmithers Rapra Publishing, Shawbury
50. Pössinger T, Bolzmacher C, Bodelot L, Triantafyllidis N (2014) Influence of interfacial adhesion on the mechanical response of magneto-rheological elastomers at high strain. Microsyst Technol 20:803–814. https://doi.org/10.1007/s00542-013-2036-0
51. Gross H, Singer W, Totzeck M (2005) Handbook of optical systems. Wiley-VCH, Berlin
52. Lefèvre, V., Danas, K., & Lopez-Pamies, O. (2017). A general result for the magnetoelastic response of isotropic suspensions of iron and ferrofluid particles in rubber, with applications to spherical and cylindrical specimens. J Mech Phys Solids 107:343–364. https://doi.org/10.1016/j.jmps.2017.06.017
53. Hashin Z (1983) Analysis of composite materials. J Appl Mech 50: 481–505. https://doi.org/10.1115/1.3167081
54. Moon FC, Pao YH (1968) Magnetoelastic Buckling of a Thin Plate. J Appl Mech 35:53–58. https://doi.org/10.1115/1.3601173
55. Rudykh S, Bertoldi K (2013) Stability of anisotropic magnetorheological elastomers in finite deformations: a micromechanical approach. J Mech Phys Solids 61:949–967. https://doi.org/10.1016/j.jmps.2012.12.008
56. Ginder J, Clark S, Schlotter W, Nichols M (2002) Magnetostrictive phenomena in magnetorheological elastomers. Int J M P B 16:2412–2418. https://doi.org/10.1142/S021797920201244X
57. Kankanala S, Triantafyllidis N (2008) Magnetoelastic buckling of a rectangular block in plane strain. J Mech Phys Solids 56:1147–1169. https://doi.org/10.1016/j.jmps.2007.10.008
58. Davis L (1999) Model of magnetorheological elastomers. J Appl Phys 85:3348–3351. https://doi.org/10.1063/1.369682
59. Han Y, Mohla A, Huang X, Hong W, Faidley LE (2015) Magnetostriction and field stiffening of magneto-active elastomers. Int J Appl Mech 7:1550001. https://doi.org/10.1142/S1758825115400013